Stress analysis of bias extension specimens

Remko Akkerman [*], Dennis Brands, Wouter J.B. Grouve

University of Twente & TPRC, Enschede, The Netherlands

ARTICLE INFO

ABSTRACT

The Bias Extension test is commonly used for material characterisation in shear, providing essential input to composites forming simulations. Specimens of different sizes are used, with some preference for the minimum length-to-width ratio of 2. A static equilibrium analysis is presented to derive the forces and stress distribution in a test specimen of this minimum aspect ratio. The stress distribution is shown to depend on two variables, while usually only one (the pulling force) is measured.

The central region of relatively longer specimens is generally subject to non-homogeneous boundary conditions, causing non-uniform deformations which can hamper accurate material characterisation. In addition, the analysis demonstrates that the major part of the pulling force is carried by the outer fibres, further emphasising the need for critical preparation and evaluation of bias extension testing if high accuracy characterisation is needed.

1. Introduction

Accurate material characterisation is key to reliable numerical predictions of material behaviour, certainly to textile and composite forming process simulations. The high anisotropy of these materials induces a range of different deformation mechanisms, each with their specific and material dependent response. For composite preforms, in-plane shear is probably the most researched deformation mechanism, followed by friction and out-of-plane bending. Standard in-plane shear tests include Picture Frame (PF) and Bias Extension (BE) experiments as benchmarked by Cao et al. [1].

In a PF test, a square piece of composite or fibre reinforcement is clamped to four hinged rigid bars with the fibres aligned with the frame. Pulling two opposite corners of the frame leads, ideally, to uniform trellis shear in the test specimen. The test is particularly sensitive to clamping and alignment errors. Careful specimen clamping makes this test a time consuming effort, especially for high temperature testing as is needed for thermoforming simulations of thermoplastic composites.

The uniaxial BE test involves extension of a rectangular fibrous specimen, with initial ±45° fibre orientation, of initial width W_0 and length $L_0 = \Lambda \cdot W_0$ (where the aspect ratio $\Lambda \geq 2$ [2]), by a pulling force F. As a result, three regions can be distinguished in the deformed specimen (A, B and C in Fig. 1) with different, but ideally homogeneous deformations per region.

The BE test can be performed more easily than the PF test, with the advantage that the fibres are not loaded in tension along the free edges of the specimen such that fibre tension does not corrupt the intended shear load. Proper interpretation of the test results is not straightforward, partially because of the heterogeneous deformations over the specimen area. Care must be taken to prevent slip in the clamps and resulting inhomogeneous strains in BE specimens, e.g. by means of specimen tabbing or the use of dog-bone shapes. Currently the test is frequently used for in-plane shear characterisation, not only for balanced woven fabrics and their thermoset or thermoplastic composites, but also for laminates of unidirectional plies [3–5], non-crimp fabrics [6] and 3D interlock fabrics [7].

Due to the heterogeneous deformations in the BE specimen, it not a trivial task to translate the test results (here, usually, force versus shear angle data) to geometry independent material property data that can be used in composites forming simulations. For this purpose, a model is needed which incorporates the evolving specimen geometry and deformation field, as well as the evolving stress distribution. Preferably, such a model is in a clear and intuitive closed form, but also parameter identification procedures may be used for this purpose, in which FE simulations of the BE test are performed iteratively until the predicted force-shear angle data approximate the measurements with sufficient accuracy. The latter, more or less black box, approach may lead to non-unique results or overfitting. This is less likely with the former approach, which may be subject to oversimplification, however, as certain assumptions need to be made to reach a sufficiently simple closed form expression. Full understanding of the measurement and the interpretation of the measurement results is crucial to material representations of high accuracy in simulations with optimum predictive

---

Nomenclature

Roman symbols

A, B, C	Deformation regions in BE specimen (Fig. 1)
F	Pulling force (N)
F_A, F_C	Pulling force acting on region A and C (N)
L_0	Initial specimen length (m)
L_k	Length of the kink lines (m)
N_A, N_C	Transverse force in region A and C (N)
N_{ij}	Internal normal force between regions i and j (N)
S_{ij}	Internal shear force between regions i and j (N)
T_i	Fibre tension on kink line segments ($i = 1 \dots 4$, see Fig. 4) (N)
u	Clamp displacement (m)
W_0	Initial specimen width (m)

Greek symbols

ε	Strain (-)
γ	Central shear angle (rad)
Λ	Specimen aspect ratio (L_0/W_0) (-)
ϕ	Local stress power per unit area ($= \tilde{\tau}\dot{\gamma}$) (W)
φ	Fibre angle in region A (rad)
$\tilde{\tau}$	Equivalent stress resultant (N/m)

Super and subscripts

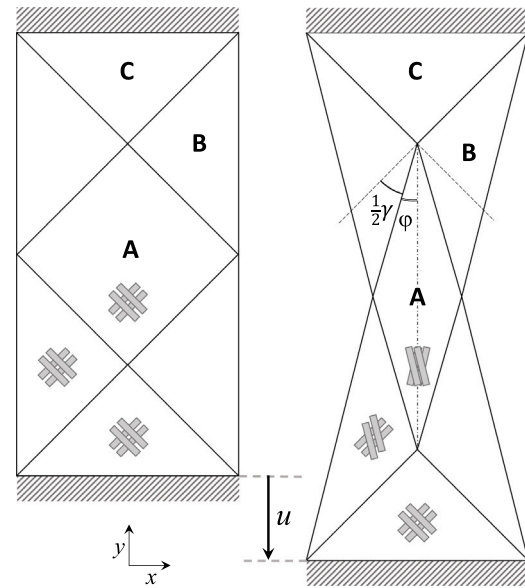|	
A, B, C	Deformation regions in specimen (Fig. 1)
x, y	Global coordinate directions, with y aligned with the pulling direction
I, II	First and second principal stress directions
$\square$	Rectangular section in region A in case specimen is extended (Fig. 6)
$\triangle$	Triangular section in region A in case specimen is extended (Fig. 6)

Fig. 1. Schematic representation of a uniaxial bias extension test of specimen with aspect ratio $\Lambda = 2$.

to measure fabric mechanical properties (in particular in shear) in 1999 [13], while the BE test was thoroughly reviewed by Boisse et al. in 2017 [14].

In the past fifty years, many authors have studied the analogies and differences between PF and BE testing. Spivak and Treloar [15] found a different resistance to shearing in both tests, concluding that "one may not simply and directly, either theoretically or empirically, obtain the complete stress–strain properties from a fabric in shear from a test in bias extension". With the development of composites forming simulations, shear characterisation of fibrous materials became of larger interest, in search of a true stress–strain relationship. Wang et al. [2] noted the minimum length for a bias extension specimen (at least twice the width) to guarantee minimum fibre tension in the central region with maximum shear. Lebrun et al. [16] derived equations to describe the kinematics of the BE test, based on the pin-jointed net assumptions and attributed differences with PF results to parasitic fibre tensions with the latter. Harrison et al. [17] introduced a power equilibrium analysis to normalise the force-shear angle data (further elaborated in [18]) and found reasonable agreement between the results of PF and BE tests. Inter-yarn slip was noted to occur at higher shear angles, not in agreement with the pin-jointed net assumptions and hence not following the ideal kinematics, leading to the recommendation of a direct measurement of the local shear angle. Launay et al. [19] derived a similar power equilibrium relation and experimentally showed that PF and BE results are very close when the tension in the picture frame is kept zero during the test. Komeili and Milani [20] confirmed the necessity of accurate shear angle measurements for a proper evaluation of the test results. Apart from inter-tow slip, Haghi Kashani et al. [21] emphasised the effect of intra-yarn shear, combined with compaction as also addressed by Xiao et al. [22].

Meso scale considerations of woven fabrics have indicated physical limits to the pin-jointed net assumptions, partially because rotation around cross-over points is hampered once the gaps between the yarns close with ongoing trellis shear, leading to yarn slip, intra-yarn shear and lateral (in-plane) yarn compression [21]. The increased resistance to shearing after reaching the locking angle leads to wrinkling [23] for both PF and BE tests, although for different global shear angles. Modifications have been proposed to extend the applicability of the kinematic model [22].

capabilities. Apart from this, fully closed form solutions for non-trivial load cases are instrumental (or even essential) for validation purposes of the same simulation methods. In this respect, closed form expressions for the heterogeneous stresses and deformations in a bias extension specimen can be most useful to identify potential deficiencies of the applied discretised solution method.

Shear testing of textiles and fibre reinforcements received growing scientific attention since the late 1940s. One of the first images of bias extension testing was shown by Weissenberg [8] while also describing trellis shear in terms of what is now known as the pin-jointed net assumptions. Chadwick [9] addressed solutions to enable uniform lateral deformations during pulling tests in the bias directions, using roller grips on an endless belt specimen or alternative clamping systems, noting issues with wrinkling, particularly in long specimens. Early bias extension measurement results were published by Cooper [10]. Kilby [11] introduced an anisotropic linear elastic model to use such measurement results for mechanical characterisation of woven fabrics.

Skelton published an early overview of fabric shear in 1976 [12], stating that (at the time) "it is probable that shear is the least understood mode of the various modes of fabric deformation". Noteworthy observations include that the number of yarn cross-over points is more significant than the thickness of a fabric, and that side-by-side contact between consecutive fibres causes a limit to shear deformation, now known as the 'locking angle'. Bassett and Postle reviewed the tests
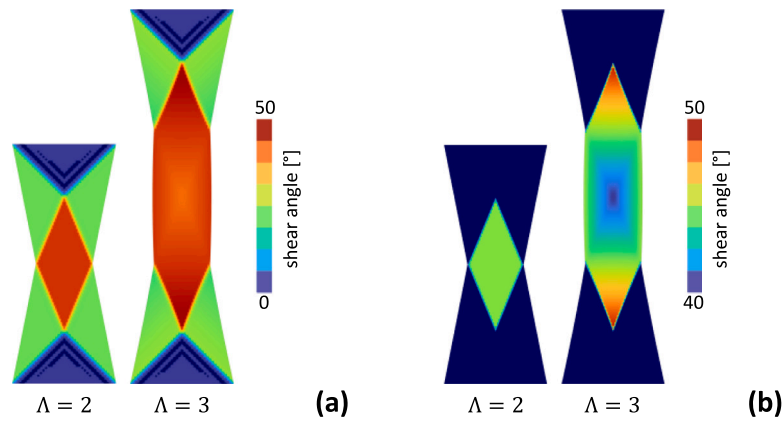
Fig. 2. Shear angle distributions in simulated bias extension specimens with a nominal shear angle of 45° for two aspect ratios (2 and 3); a) over the full strain range from 0° to 50°; b) within a limited strain window from 40° to 50° (shear angles outside the range are plotted in grey). The material properties and boundary conditions are as specified in Tables 1 and 2.

Also on the macroscopic scale not all earlier doubts and questions have been fully resolved to date, for instance as addressed in [24], making it difficult to interpret the measurement results unambiguously. The solution for specimens of very long length [25] was found for specimens of finite length ($2 < \varLambda < \infty$) when elaborating stress equilibrium with free boundary conditions along the specimen's edges [24,26]. This differs from the commonly accepted power equilibrium solution [1,18,19,27].

In addition to these contradicting observations, numerical simulations of BE experiments show specimen size dependent strain gradients. Only for the minimum length-to-width ratio ($\varLambda = 2$) the predicted shear angles are piecewise uniform, which is not the case for larger aspect ratios. Fig. 2 shows the predicted shear angle distribution for $\varLambda = 2$ and 3 for a biaxially reinforced carbon/PEEK material for equal nominal strain and strain rate (ideally leading to 45° shear), simulated using the Aniform implicit Finite Element (FE) software [28]. The specimens, with an initial width of 100 mm and initial lengths of 200 mm and 300 mm, respectively, were modelled with a regular grid of fibre aligned linear triangular elements with shortest edge lengths of 2.5 mm. The deformations shown here were found to be converged with mesh refinement. Strain gradients become apparent for the larger aspect ratio when a sufficiently narrow window is chosen for the displayed strain levels (Fig. 2b). Nonetheless, the deformations of the elements were as to be expected for trellis shear, with negligible fibre strains (less than 0.008%). Varying the specimen's aspect ratio from 2 to 5 leads to further shear variations along the specimen's longitudinal axis of symmetry, as illustrated in Fig. 3. Such strain variations complicate the use of the test for accurate material characterisation. The results presented here will be addressed in more detail in the later part of this paper.

To clarify the effects of specimen sizes and boundary conditions, a macroscopic equilibrium analysis of a BE specimen will be elaborated, firstly for $\varLambda = 2$. All forces and stress resultants are mutually related by means of the equilibrium equations. It will be shown that, for a given deformation field, two of the independent variables must be known (which can be any pair) to determine all other variables, while usually only one of those is measured during the test (the pulling force exerted on the specimen). This confirms the need for additional assumptions or instrumentation to permit quantitative interpretation of the measurements. The power equilibrium solution can be derived from this analysis, also for specimens of larger aspect ratios. Not only the pulling force, but also all other forces can be expressed in terms of the equivalent stress resultants in region A and B. These results serve a proper understanding of the limitations of the simple theories for BE specimens of intermediate length and promote awareness of the pitfalls in translation of BE test results to material property data for constitutive models in process simulations.
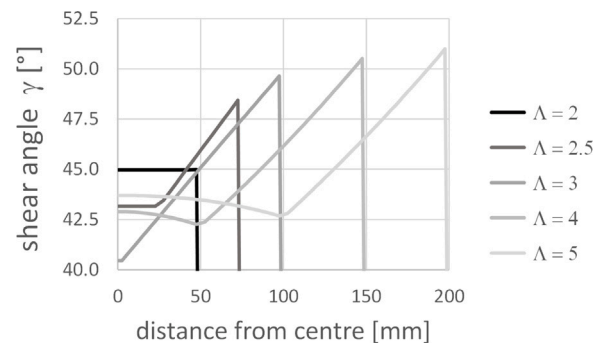

Fig. 3. Shear angle distributions in simulated bias extension specimens of initial width $W_0 = 100$ mm with a nominal shear angle of 45° for aspect ratios from 2 to 5, plotted versus the initial coordinates along the longitudinal axis from centre ($y = 0$) to edge ($y = L/2$). The vertical lines mark the transition from the central region A to the undeformed region C. The material properties and boundary conditions are in conformance with Tables 1 and 2, respectively.

2. Theory

After a summary of the kinematics of the BE test, a system of equilibrium equations will be derived, from which the internal forces in a BE specimen of minimum length can be solved. These forces will be translated to the stress resultants in the three distinct regions of the specimen. The results will then be further elaborated for specimens of a larger aspect ratio.

2.1. Kinematic relations and their limitations

Before going into details, the kinematics of the BE test will be briefly recapitulated, which are the basis for the common theories used for analyses of the test results to obtain material property data. The common underlying simplifications and assumptions are:

1. The fibres are inextensible;
2. There is no slip between the fibres and the clamping is perfect;
3. The bending stiffness of the fibres is negligible;
4. The deformations are uniform within all three distinct regions of the BE specimen;

which imply pure trellis shear deformations without slippage. As a result of these assumptions, region C cannot be deformed and the initial length-to-width ratio must satisfy $\varLambda \geq 2$. The fibre angle φ in the central region A, with respect to the longitudinal axis of the specimen,

is related to the central shear angle γ by

$$\frac{1}{2}\pi = 2\varphi + \gamma. \tag{1}$$

In the absence of slip, the clamp displacement u (and elongation of region A) is related to the fibre angle by

$$\frac{u}{W_0} = (\Lambda - 1) \cdot \left(\sqrt{2}\cos\varphi - 1\right), \tag{2}$$

leading to the shear rate in region A equal to

$$\dot{\gamma} = -2\dot{\varphi} = \frac{\sqrt{2}}{(\Lambda - 1)\sin\varphi} \cdot \frac{\dot{u}}{W_0}. \tag{3}$$

The shear angle and shear rate in region B are half of their respective counterparts in region A, while both are equal to zero in region C.

This kinematic model of pure trellis shear or the pin-jointed net approach is known to have practical limitations. Tow-tow slippage may occur at the free edges of a BE specimen [2]. The small but finite bending rigidity of the fibres prevents a discrete step in shear deformation between two regions, although in-plane bending is negligible if the specimen size is large enough [29]. Slip between the clamps and the specimen occurs easily during BE testing. All these effects lead to inhomogeneous deformations which need to be eliminated or corrected for to make the test results suitable for interpretation using the standard kinematics, for instance by directly measuring the local shear angle. In addition to this we have shown an effect of the specimen's aspect ratio, which can be explained from a basic equilibrium analysis.

2.2. Equilibrium of forces and moments

The equilibrium analysis (neglecting inertial effects) starts from the common assumptions, mentioned above. Thus, a BE specimen can be subdivided into triangular or quadrilateral areas of homogeneous deformation, separated by individual fibres between different regions. Here we will analyse the limit case $\Lambda = 2$ such that region A is fully surrounded by regions B.

Consider a quarter of the Bias Extension specimen, see Fig. 4. The three regions A, B and C are represented, together with the fibres on the lines separating the three areas, denoted as the kink lines. Here, these kink lines are considered to be straight wires under non-uniform tension. We will address each region and kink line one by one.

Region A: The shear forces on the legs of the right triangle in region A must be zero due to symmetry conditions. As a result, equilibrium of moments taken around the centre of the hypotenuse is satisfied automatically for all values of F_A, N_A, N_{AB} and S_{AB}. In other words, equilibrium of moments does not add any other constraint than already implied by force equilibrium,

$$\begin{aligned} \Sigma F_x = 0 \Rightarrow \quad & N_A = N_{AB} \cdot \cos\varphi - S_{AB} \cdot \sin\varphi, \\ \Sigma F_y = 0 \Rightarrow \quad & \tfrac{1}{2}F_A = N_{AB} \cdot \sin\varphi + S_{AB} \cdot \cos\varphi. \end{aligned} \tag{4}$$

The legs of the triangle coincide with the principal stress directions in this region. In the absence of tension in the outer end of the yarn corresponding to kink line A/B ($T_1 = 0$), the pulling force on region A equals the external force, $F_A = F$.

Region B: The base of this isosceles triangle is the free edge of the BE specimen, with zero shear and normal forces. The equilibrium equations read (considering moment equilibrium around the top of the triangle):

$$\begin{aligned} \Sigma F_x = 0 \Rightarrow \quad & \tfrac{1}{2}\sqrt{2} \cdot \left(-N_{BC} + S_{BC}\right) = N_{BA} \cdot \cos\varphi - S_{BA} \cdot \sin\varphi, \\ \Sigma F_y = 0 \Rightarrow \quad & \tfrac{1}{2}\sqrt{2} \cdot \left(N_{BC} + S_{BC}\right) = N_{BA} \cdot \sin\varphi + S_{BA} \cdot \cos\varphi, \\ \Sigma M = 0 \Rightarrow \quad & N_{BC} = N_{BA}. \end{aligned} \tag{5}$$

Region C: As for Region A, the shear forces on the legs of triangle C must be zero due to symmetry conditions. Similarly, equilibrium of
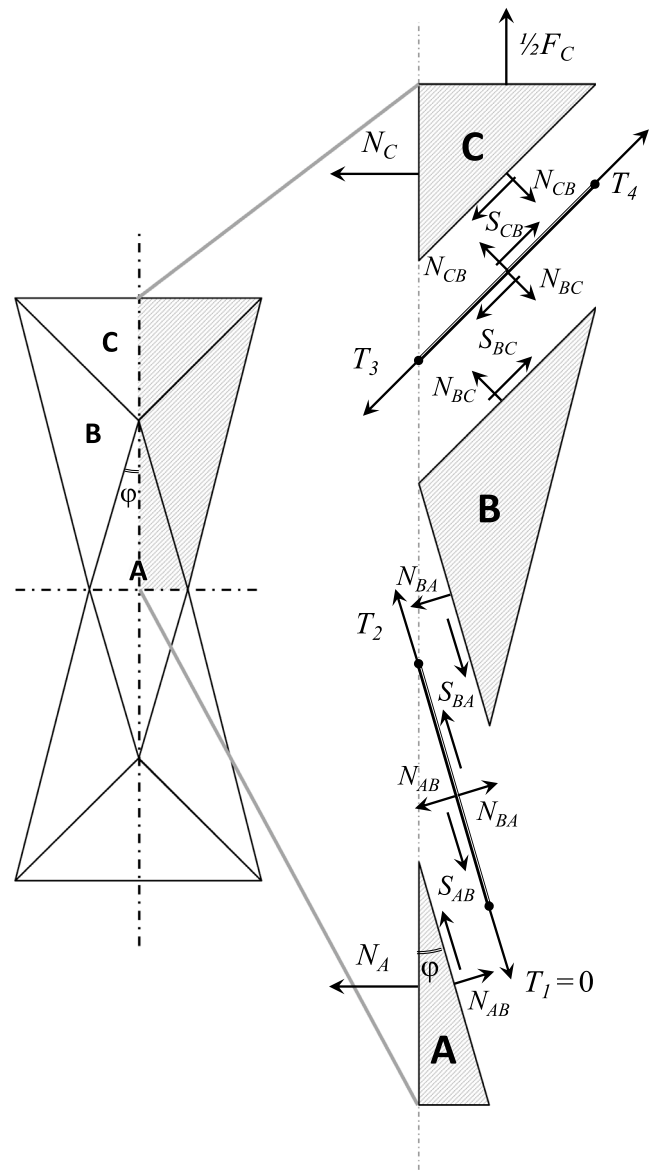

Fig. 4. Free Body Diagrams of the separated regions and lines of discontinuity, illustrating the internal normal forces N_{ij}, internal shear forces S_{ij}, external forces F_i and fibre tensions T_i.

moments is satisfied automatically for all values of F_C, N_C, N_{CB} and S_{CB}.

$$\begin{aligned} \Sigma F_x = 0 \Rightarrow \quad & N_C = \tfrac{1}{2}\sqrt{2} \cdot \left(N_{CB} - S_{CB}\right), \\ \Sigma F_y = 0 \Rightarrow \quad & \tfrac{1}{2}F_C = \tfrac{1}{2}\sqrt{2} \cdot \left(N_{CB} + S_{CB}\right). \end{aligned} \tag{6}$$

Kink line A/B: Tension can build up in the yarn on this kink line, due to the discontinuous shear when crossing this line. The tension must be zero at the free edge of the specimen, $T_1 = 0$. This yarn has zero resistance against normal forces, such that force equilibrium in tangential and normal directions read, respectively,

$$\begin{aligned} \Sigma F_t = 0 \Rightarrow \quad & T_2 = S_{AB} - S_{BA}, \\ \Sigma F_n = 0 \Rightarrow \quad & N_{AB} = N_{BA}. \end{aligned} \tag{7}$$

Kink line B/C: Similar arguments as above, now with a clamping condition at the edge of the specimen, lead to force equilibrium

conditions in tangential and normal directions, respectively,

$$\Sigma F_t = 0 \Rightarrow \quad T_4 - T_3 = S_{BC} - S_{CB}, \tag{8}$$

$$\Sigma F_n = 0 \Rightarrow \qquad N_{BC} = N_{CB}.$$

At the cross-over point the fibres on both kink lines can transfer their tension mutually, subject to force equilibrium. Equilibrium in the x-direction is secured by symmetry conditions, whereas kink line force equilibrium in the y-direction implies

$$\Sigma F_y = 0 \Rightarrow \quad \tfrac{1}{2}\sqrt{2} \cdot T_3 = T_2 \cdot \cos\varphi. \tag{9}$$

It can be shown that the combination of the foregoing 12 equations (including $T_1 = 0$ and hence $F_A = F$, the known externally applied force) satisfies force and moment equilibrium (around the triple point) of the entire system of elements,

$$\begin{aligned}
\Sigma F_x = 0 \quad &\Rightarrow \quad \tfrac{1}{2}\sqrt{2} \cdot T_4 + T_1 \sin\varphi = \\
&= N_C + \tfrac{1}{2}\sqrt{2} \cdot T_3 + T_2 \cdot \sin\varphi + N_A, \\
\Sigma F_y = 0 \quad &\Rightarrow \quad \tfrac{1}{2}F_C + \tfrac{1}{2}\sqrt{2} \cdot T_4 = \tfrac{1}{2}F, \\
\Sigma M = 0 \quad &\Rightarrow \quad \tfrac{1}{2}F_C + N_C = \sqrt{2}N_A \cos\varphi + \tfrac{1}{2}\sqrt{2}F \sin\varphi.
\end{aligned} \tag{10}$$

These do not add any further constraints to the overall solution, leaving two of the 14 variables (N_{AB}, N_{BA}, N_{BC}, N_{CB}, S_{AB}, S_{BA}, S_{BC}, S_{CB}, N_A, N_C, F_C, T_2, T_3, T_4) as unknowns. Observing the linearity of the system of equations, it is legitimate to choose various combinations of two driving forces, as long as these are mutually independent. Here, we leave S_{CB} and N_A as unknowns when solving for the other 12 below.

2.3. Solutions of the forces

Solving the total system of Eqs. (4)–(9) leads to the following results. *Normal forces between the regions:*

$$N_{AB} = N_{BA} = N_{BC} = N_{CB} = \sin\varphi \cdot \tfrac{1}{2}F + \cos\varphi \cdot N_A, \tag{11}$$

Observing that region B is an isosceles triangle with zero shear and normal force on the base edge it can be confirmed that both the shear and normal forces on the legs must be symmetric. *Shear forces between the regions:*

$$S_{AB} = \cos\varphi \cdot \tfrac{1}{2}F - \sin\varphi \cdot N_A, \tag{12}$$

$$S_{BC} = S_{BA} = \frac{\sqrt{2} + \cos\varphi - \sin\varphi}{\cos\varphi + \sin\varphi}\left(\sin\varphi \cdot \tfrac{1}{2}F + \cos\varphi \cdot N_A\right), \tag{13}$$

with the latter being proportional to the previously solved normal forces $N_{AB} = N_{BA} = N_{BC} = N_{CB}$, for a given fibre angle φ. *Kink line tensions:*

$$T_2 = \frac{1}{\cos\varphi + \sin\varphi}\left((1 - \sqrt{2}\sin\varphi) \cdot \tfrac{1}{2}F - (1 + \sqrt{2}\cos\varphi) \cdot N_A\right), \tag{14}$$

$$T_3 = \frac{\cos\varphi}{\cos\varphi + \sin\varphi}\left((\sqrt{2} - 2\sin\varphi) \cdot \tfrac{1}{2}F - (\sqrt{2} + 2\cos\varphi) \cdot N_A\right), \tag{15}$$

$$T_4 = (\sqrt{2} - \sin\varphi) \cdot \tfrac{1}{2}F - \cos\varphi \cdot N_A - S_{CB}. \tag{16}$$

Loads on Region C:

$$N_C = \tfrac{1}{2}\sqrt{2}\left(\sin\varphi \cdot \tfrac{1}{2}F + \cos\varphi \cdot N_A - S_{CB}\right), \tag{17}$$

$$F_C = \sqrt{2}\left(\sin\varphi \cdot \tfrac{1}{2}F + \cos\varphi \cdot N_A + S_{CB}\right). \tag{18}$$

The resulting expressions (11)–(18) show that only the forces related to region C and kink line B/C (i.e. N_C, F_C and T_4) are dependent on the shear force S_{CB}. All other variables can be expressed in only the external force F and normal force N_A, related to, respectively, the longitudinal and transverse stress in region A. Strictly, there is no prior knowledge on the value of S_{CB}. It can be argued, however, that with zero shear and a zero shear rate in region C also the shear stress (and thus the shear force S_{CB}) must be zero, leaving also the three mentioned forces a function of F and N_A only, i.e.

$$F_C = 2N_C = \sqrt{2}N_{AB}, \tag{19}$$

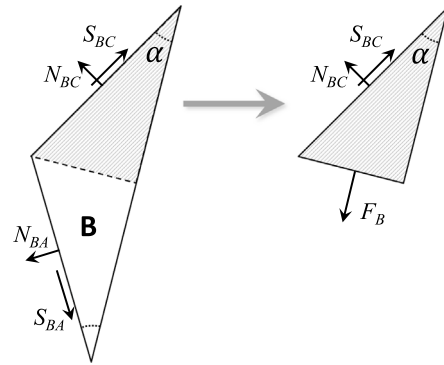which further simplifies the solution of the system of equations.

Fig. 5. Force in the principal stress direction of Region B.

2.4. Stress resultants

The piecewise uniform shear and shear rates lead to a uniform state of stress and stress resultants for each of the three regions. Consequently, the stress resultants (or: "thickness integrated stresses" or "forces per unit width") in each region are directly related to the forces considered above. Using the notation and dimensions introduced in [24], we can derive the following results. The side lengths of the regions are proportional to the initial width of the specimen W_0, as both kink lines have a constant length

$$L_k = \tfrac{1}{2}\sqrt{2}\, W_0. \tag{20}$$

The principal directions I and II of the stress resultant τ in region A coincide with the global $x-$ and $y-$coordinate system. This implies that

$$\begin{aligned}
\tau_I^A = \tau_y^A \quad &= \quad \frac{\tfrac{1}{2}F}{L_k \sin\varphi} = \frac{\sqrt{2}}{\sin\varphi}\frac{\tfrac{1}{2}F}{W_0}, \\
\tau_{II}^A = \tau_x^A \quad &= \quad \frac{N_A}{L_k \cos\varphi} = \frac{\sqrt{2}}{\cos\varphi}\frac{N_A}{W_0}.
\end{aligned} \tag{21}$$

Hence, the forces F and N_A are proportional to the principal stress resultants in the central region A and thus fully define the local stress resultant state in this region. Note the difference with the result obtained earlier in [24] as now a non zero transverse stress is permitted. The equivalent stress resultant, following from the local stress power per unit area ϕ ($\tilde{\tau} = \phi/\dot{\gamma}$), can be expressed as (according to Eq. (34) in [24])

$$\tilde{\tau}^A = \tfrac{1}{2}\left(\tau_I^A \tan\varphi - \frac{\tau_{II}^A}{\tan\varphi}\right), \tag{22}$$

which now leads to

$$\tilde{\tau}^A = \frac{\sqrt{2}}{2W_0}\left(\frac{\tfrac{1}{2}F}{\cos\varphi} - \frac{N_A}{\sin\varphi}\right). \tag{23}$$

Region B is in a state of uniaxial stress, with the principal stress directions parallel and normal to the free edge. Considering the upper half of this triangle (see Fig. 5), it is found straightforwardly that the normal force acting on the axis of symmetry equals

$$F_B = \sin\alpha \cdot N_{BC} + \cos\alpha \cdot S_{BC}. \tag{24}$$

With zero forces acting on the free edge, the forces on edge BC must satisfy

$$\cos\alpha \cdot N_{BC} - \sin\alpha \cdot S_{BC} = 0, \tag{25}$$

such that F_B can also be expressed as

$$F_B = \frac{S_{BC}}{\cos\alpha}. \tag{26}$$

The first principal stress resultant in region B follows as

$$\tau_I^B = \frac{F_B}{L_k \sin \alpha} = \frac{\sqrt{2}}{\sin \alpha} \frac{F_B}{W_0} = \frac{\sqrt{2}}{\sin \alpha \cos \alpha} \frac{S_{BC}}{W_0}. \tag{27}$$

As the second principal stress $\tau_{II}^B = 0$, the equivalent stress resultant is found as

$$\tilde{\tau}^B = \frac{1}{2} \tau_I^B \tan \alpha = \frac{\sqrt{2}}{2 \cos^2 \alpha} \frac{S_{BC}}{W_0} = \frac{2}{\sqrt{2} + \cos \varphi - \sin \varphi} \frac{S_{BC}}{W_0}. \tag{28}$$

Using the results of the previous section we may substitute (13) into (28), leading to

$$\tilde{\tau}^B = \frac{2}{(\cos \varphi + \sin \varphi) \cdot W_0} \left(\sin \varphi \cdot \frac{1}{2} F + \cos \varphi \cdot N_A \right) \tag{29}$$

and conclude that also the equivalent stress resultants $\tilde{\tau}^A$ and $\tilde{\tau}^B$ can be expressed in terms of F and N_A (or the corresponding stress components).

2.5. Forces in terms of stress resultants

Instead of a system of equations in terms of forces, we can formulate these relations in terms of the equivalent stress resultants $\tilde{\tau}^A$ and $\tilde{\tau}^B$ as the independent variables. The full response of a BE specimen can be described explicitly once a constitutive equation $\tilde{\tau}(\gamma, \dot{\gamma})$ has been specified, given the earlier assumed shear angles ($\gamma^A = \gamma, \gamma^B = \frac{1}{2} \gamma$) and shear rates ($\dot{\gamma}^A = \dot{\gamma}, \dot{\gamma}^B = \frac{1}{2} \dot{\gamma}$).

Linear combination of the earlier results, in particular the equivalent stress resultants (23), (29) and the solutions (11)–(19), leads to

$$
\begin{aligned}
F &= \left(\sqrt{2} \cos \varphi \cdot \tilde{\tau}^A + \frac{1}{2} \left(1 + \frac{1}{\tan \varphi} \right) \cdot \tilde{\tau}^B \right) \cdot W_0, \\
N_A &= \left(-\sqrt{2} \sin \varphi \cdot \tilde{\tau}^A + \frac{1}{2} (1 + \tan \varphi) \cdot \tilde{\tau}^B \right) \cdot \frac{1}{2} W_0, \\
F_C &= \frac{1}{2} \sqrt{2} (\cos \varphi + \sin \varphi) \tilde{\tau}^B \cdot W_0, \\
S_{BC} &= \frac{1}{2} \left(\sqrt{2} + \cos \varphi - \sin \varphi \right) \tilde{\tau}^B \cdot W_0, \\
T_4 &= \cos \varphi \cdot W_0 \tilde{\tau}^A + \frac{1}{4} \sqrt{2} (\sin \varphi + \cos \varphi) \left(\frac{1}{\sin \varphi} - \sqrt{2} \right) \cdot W_0 \tilde{\tau}^B.
\end{aligned}
\tag{30}
$$

These equations show that a constitutive relation or assumption is needed to determine the internal forces if only the pulling force F and the fibre angle φ are known. Also the remaining terms of the full field solution of the stress resultants in all three regions can be expressed in terms of $\tilde{\tau}_A$ and $\tilde{\tau}_B$, as addressed in the Appendix.

2.6. Power equilibrium for minimum and longer length specimens

The relation between the pulling force F, the central fibre angle φ, and the equivalent stress resultants $\tilde{\tau}$ in region A and B given in (30) can be reformulated as

$$\sqrt{2} \sin \varphi \cdot \frac{F}{W_0} = \sin 2\varphi \cdot \tilde{\tau}^A + \frac{1}{2} \sqrt{2} (\cos \varphi + \sin \varphi) \cdot \tilde{\tau}^B. \tag{31}$$

This is consistent with the earlier mentioned result of the power equilibrium approach [1,24,26,27],

$$(\Lambda - 1) \sqrt{2} \sin \varphi \cdot \frac{F}{W_0} = (2\Lambda - 3) \sin 2\varphi \cdot \tilde{\tau}^A + \frac{1}{2} \sqrt{2} (\cos \varphi + \sin \varphi) \cdot \tilde{\tau}^B, \tag{32}$$

or, when expressed in terms of the shear angle γ (where it may be noted that the "shear force per unit length" and the "equivalent stress resultant" are interchangeable, see [24]),

$$(\Lambda - 1) \left(\cos \frac{1}{2} \gamma + \sin \frac{1}{2} \gamma \right) \cdot \frac{F}{W_0} = (2\Lambda - 3) \cos \gamma \cdot \tilde{\tau}^A + \cos \frac{1}{2} \gamma \cdot \tilde{\tau}^B, \tag{33}$$

where in the current case the aspect ratio equals $\Lambda = 2$. With the force equilibrium analysis, we now also have the expressions for all other forces and stress resultants available. This can be most useful for a better understanding and validation of numerical simulation results, but also highlights and explains other phenomena, as will be shown below.
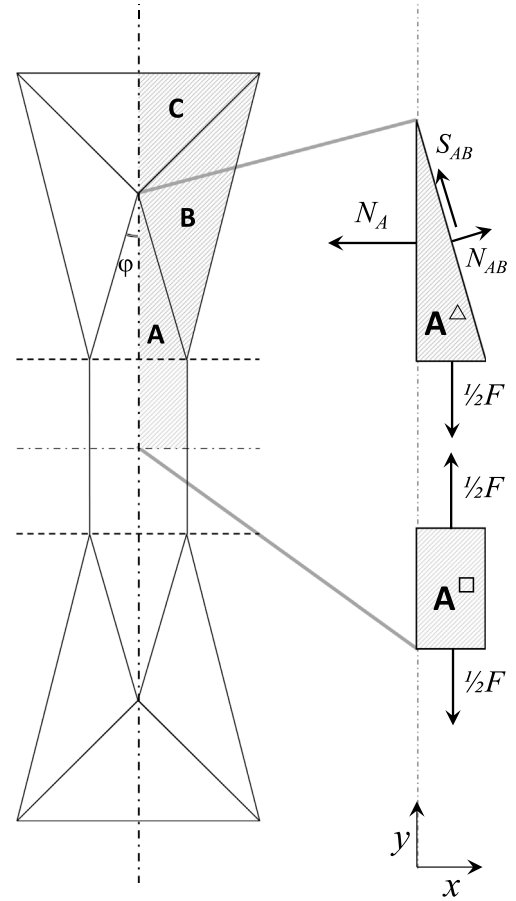

Fig. 6. Extension of the length of a BE specimen by adding Region $A^{\square}$ in the centre.

Considering specimens of longer length (i.e. $\Lambda > 2$), the central region may be artificially extended with a rectangular region $A^{\square}$ (see Fig. 6), with initial length $(\Lambda - 2)W_0$. According to the original assumptions, the deformation in the added region $A^{\square}$ is supposed to be equal to the deformation in the neighbouring triangle $A^{\triangle}$. The loading condition may well be different, however, as $A^{\square}$ is subjected to only the uniaxial pulling load F as elaborated previously [24,26].

Taking the area average of the equivalent stress resultant in Region A under these assumptions, we find

$$
\begin{aligned}
\bar{\tilde{\tau}}^A &= \frac{A^{\triangle}}{A^{\triangle} + A^{\square}} \cdot \tilde{\tau}^{\triangle} + \frac{A^{\square}}{A^{\triangle} + A^{\square}} \cdot \tilde{\tau}^{\square} = \\
&= \frac{\frac{1}{8} W_0^2}{\frac{1}{8} (2\Lambda - 3) W_0^2} \cdot \frac{\sqrt{2}}{2 W_0} \left(\frac{\frac{1}{2} F}{\cos \varphi} - \frac{N_A}{\sin \varphi} \right) + \\
&\quad + \frac{\frac{1}{4} (\Lambda - 2) W_0^2}{\frac{1}{8} (2\Lambda - 3) W_0^2} \cdot \frac{\sqrt{2}}{2 W_0} \left(\frac{\frac{1}{2} F}{\cos \varphi} \right) = \\
&= \frac{\sqrt{2}}{2 W_0} \left(\frac{\frac{1}{2} F}{\cos \varphi} - \frac{N_A}{(2\Lambda - 3) \sin \varphi} \right).
\end{aligned}
\tag{34}
$$

Combining (34) with (29) and eliminating N_A now leads to the original power equilibrium result (32) for arbitrary specimen length. This is not surprising, as both elaborations are based on the same assumptions. Note that the current result is not restricted to rate independent behaviour, as indicated earlier for the power equilibrium result [25].

Now, we have more detailed background information to the previous power-based analyses. In the general case transverse stresses are generated between the regions A and B ($N_A \neq 0$) such that the central area A of a longer specimen ($\Lambda > 2$) is subject to non

uniform boundary conditions. This was overlooked in previous publications [24,26] where homogeneous boundary conditions were assumed. The final result derived there hence only applies to very long specimens ($\Lambda \to \infty$). Revisiting the original assumptions of both analyses, it is counterintuitive to assume equal deformations between the two sub regions subject to a different transverse load. Depending on the sign of the transverse force N_A, the free section is expected to become wider or narrower than the triangle between regions B. This also explains the strain gradients in numerical simulations of longer length specimens. For a compressive transverse load, the shear angle will be highest in $A^{\triangle}$ and decrease towards $A^{\square}$.

3. Application of the theoretical results

Reviewing the results derived so far, it is obvious that in-plane shear characterisation by means of BE tests on minimum length specimens requires more than only measuring the pulling force versus the shear angle data. This can be resolved by proposing additional assumptions, such as rate independent material behaviour, leading to a relation between the equivalent stress resultants in regions A and B. If this relation is specified by e.g. $\tilde{\tau}(\gamma) = \sum_i^n c_i N_i(\gamma)$ with shear angle γ, using constants c_i and shape functions $N_i(\gamma)$ (polynomials, for instance), then these constants can be determined by direct linear least squares fitting of the force versus shear angle data (33), without having to use iterative techniques as described previously [18,26,29]. The assumption of rate independency is not applicable to prepregs and laminates in general, with the viscous matrix inducing a rate dependent response during the forming stage.

Measuring other forces would complicate the experiment, although it could be attempted to mount the specimen in segmented clamps by which the tension in the outer fibres at the clamped edge T_4 and the remaining pulling force in the clamped region F_C could be distinguished and thus provide the missing information. Certainly for high temperature measurements such clamping would seem highly impractical, however.

Nonetheless, the findings above can be exploited in alternative manners. We will discuss the assumption of initial material linearity and the combination of measurement results for different specimen lengths. The latter will be validated against numerical simulations and evaluated for their applicability in experimental practice.

3.1. Linearity

Many materials, whether of an elastic, viscous or viscoelastic nature, behave in a linear fashion for small deformations (i.e. the force or stress as a function of the displacement, strain, velocity or strain rate). In this case, we could expect the force to depend linearly on the crosshead displacement and/or velocity, or respectively on the shear angle and/or shear rate. Observing that the shear angle and the shear rate in region B are half of their respective counterparts in region A, we can explore the effect of such linearity. The effect that fibre tension might have on the shear response of the material under consideration is neglected here, noting that fibre tension is relatively low for uniaxial BE testing. In case the onset (i.e. when $\varphi = \frac{1}{4}\pi$) of the material response to loading is linear in the sense that $\lim_{\varphi \to \frac{\pi}{4}} \tilde{\tau}^B = \frac{1}{2}\tilde{\tau}^A$, then with (30) the pulling force F and the central equivalent stress resultant $\tilde{\tau}^A$ initially relate according to

$$\lim_{\varphi \to \frac{\pi}{4}} \frac{W_0 \tilde{\tau}^A}{F} = \lim_{\varphi \to \frac{\pi}{4}} \frac{1}{\sqrt{2}\cos\varphi + \frac{1}{4}\left(1 + \frac{1}{\tan\varphi}\right)} = \frac{2}{3}, \tag{35}$$

which provides a simple first estimate of the underlying material response (i.e. the equivalent stress resultant) to shear deformation. The

ratios between the other forces and F for small shear angles then straightforwardly follow as

$$\lim_{\varphi \to \frac{\pi}{4}} \frac{N_A}{F} = \lim_{\varphi \to \frac{\pi}{4}} \frac{1 - 4\sqrt{2}\sin\varphi + \tan\varphi}{2 + 8\sqrt{2}\cos\varphi + 2\frac{1}{\tan\varphi}} = -\frac{1}{6},$$

$$\lim_{\varphi \to \frac{\pi}{4}} \frac{F_C}{F} = \lim_{\varphi \to \frac{\pi}{4}} \frac{1}{2}\sqrt{2}(\cos\varphi + \sin\varphi)\cdot\frac{1}{3} = \frac{1}{3},$$

$$\lim_{\varphi \to \frac{\pi}{4}} \frac{S_{BC}}{F} = \lim_{\varphi \to \frac{\pi}{4}} \frac{1}{2}\left(\sqrt{2} + \cos\varphi - \sin\varphi\right)\cdot\frac{1}{3} = \frac{1}{6}\sqrt{2}, \tag{36}$$

$$\lim_{\varphi \to \frac{\pi}{4}} \frac{T_4}{F} = \lim_{\varphi \to \frac{\pi}{4}} \frac{\sqrt{2} + 6\cos\varphi + \frac{\sqrt{2}}{\tan\varphi} - 2\sin\varphi}{2 + 8\sqrt{2}\cos\varphi + 2\frac{1}{\tan\varphi}} = \frac{1}{3}\sqrt{2},$$

which shows initial transverse compression in region A (i.e. $N_A < 0$). Further, the second relation shows that the pulling force on region C is only $\frac{1}{3}$ of the applied pulling force F, which means that $\frac{2}{3}$ of the pulling force is transferred to the clamps by the outer fibres by means of T_4, clearly explaining the issues with proper clamping during a BE test.

Further, using (21) this translates to

$$\lim_{\varphi \to \frac{\pi}{4}} \frac{\tau_x^A}{\tau_y^A} = -\frac{1}{3}, \tag{37}$$

implying that the stress state in region A is biaxial (longitudinal tension + transverse compression) from the beginning for initially linear material behaviour. This ratio between the normal stresses can be observed to be different for other loading conditions: for PF specimens it is -1 [24,30] while it is 0 for the BE long length solution ($\Lambda \to \infty$) [24], in this respect confirming the earlier quoted statement of Spivak and Treloar on the difference between (PF) shear and bias extension.

3.2. Exploiting different length solutions

Noting that the relation between the pulling force and the equivalent stress resultant depends on the aspect ratio Λ, see (31) and (32), the pulling force may be measured for e.g. $\Lambda = 2$ and $\Lambda = 3$, leading to, respectively,

$$\sqrt{2}\sin\varphi\cdot\frac{F_{(2)}}{W_0} = \sin 2\varphi\cdot\tilde{\tau}^A + \frac{1}{2}\sqrt{2}(\cos\varphi + \sin\varphi)\cdot\tilde{\tau}^B,$$

$$2\sqrt{2}\sin\varphi\cdot\frac{F_{(3)}}{W_0} = 3\sin 2\varphi\cdot\tilde{\tau}^A + \frac{1}{2}\sqrt{2}(\cos\varphi + \sin\varphi)\cdot\tilde{\tau}^B. \tag{38}$$

If the equivalent stress resultants are equal in both cases (i.e. the relevant state variables such as γ, $\dot{\gamma}$ are equal for both tests), then subtraction leads to

$$\sqrt{2}\sin\varphi\cdot\left(2\frac{F_{(3)}}{W_0} - \frac{F_{(2)}}{W_0}\right) = 2\sin 2\varphi\cdot\tilde{\tau}^A, \tag{39}$$

which gives an explicit expression for the central stress resultant as a function of the fibre angle φ and the forces measured on the two different specimens,

$$\tilde{\tau}^A = \frac{\sqrt{2}}{4\cos\varphi}\cdot\left(2\frac{F_{(3)}}{W_0} - \frac{F_{(2)}}{W_0}\right). \tag{40}$$

This approach bears clear similarity to the approach proposed in [20], but now including rate dependent materials. A similar procedure can be used for all other dependent variables. For example, by means of (23) the transverse force for the minimum length solution follows as

$$N_{A(2)} = \tan\varphi\left(F_{(2)} - F_{(3)}\right) \tag{41}$$

and the corresponding principal stress resultants in the central region, using (21),

$$\tau_I^A = \frac{\frac{1}{2}\sqrt{2}}{\sin\varphi}\cdot\frac{F_{(2)}}{W_0},$$

$$\tau_{II}^A = \frac{\sqrt{2}\sin\varphi}{\cos^2\varphi}\cdot\frac{F_{(2)} - F_{(3)}}{W_0}. \tag{42}$$
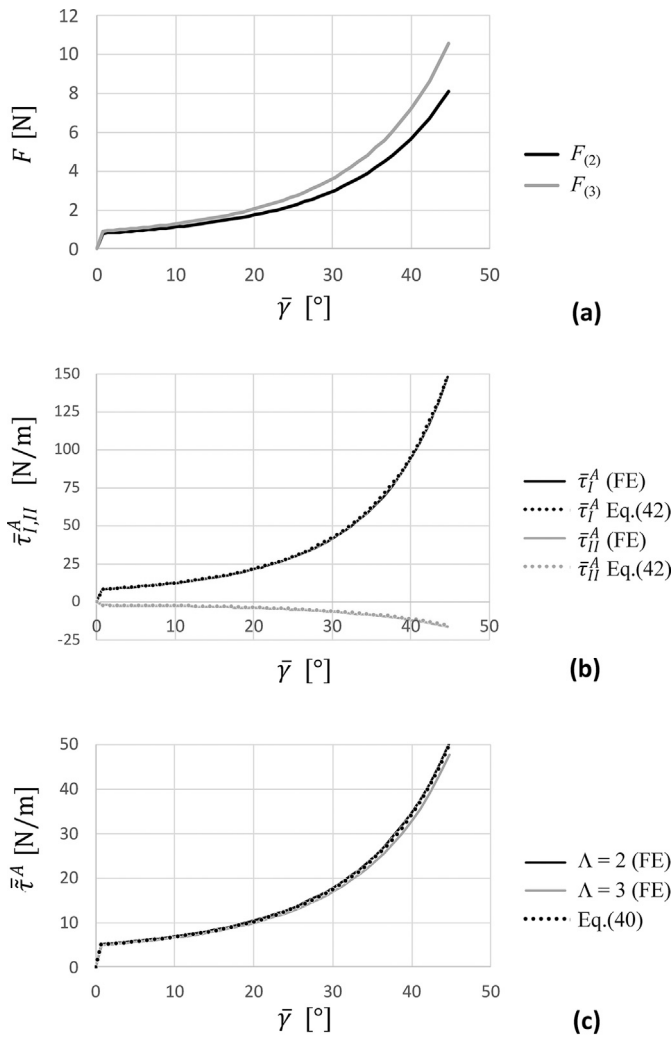
Fig. 7. FE simulation results for bias extension specimens with aspect ratios Λ of 2 and 3, plotted against the area averaged shear angle $\bar{\gamma}$ in region A: (a) predicted pulling forces; (b) principal stress resultants averaged over all elements in region A for $\Lambda = 2$ versus the values predicted from the pulling forces using Eq. (42); (c) area averaged equivalent stress resultants in region A, following from the principal values in all finite elements in this region, versus the values predicted from the pulling forces using Eq. (40).

Table 1

Material property data for Finite Element simulations using the Aniform composites forming software. The corresponding constitutive equations for fabric reinforcement are reported in [31].

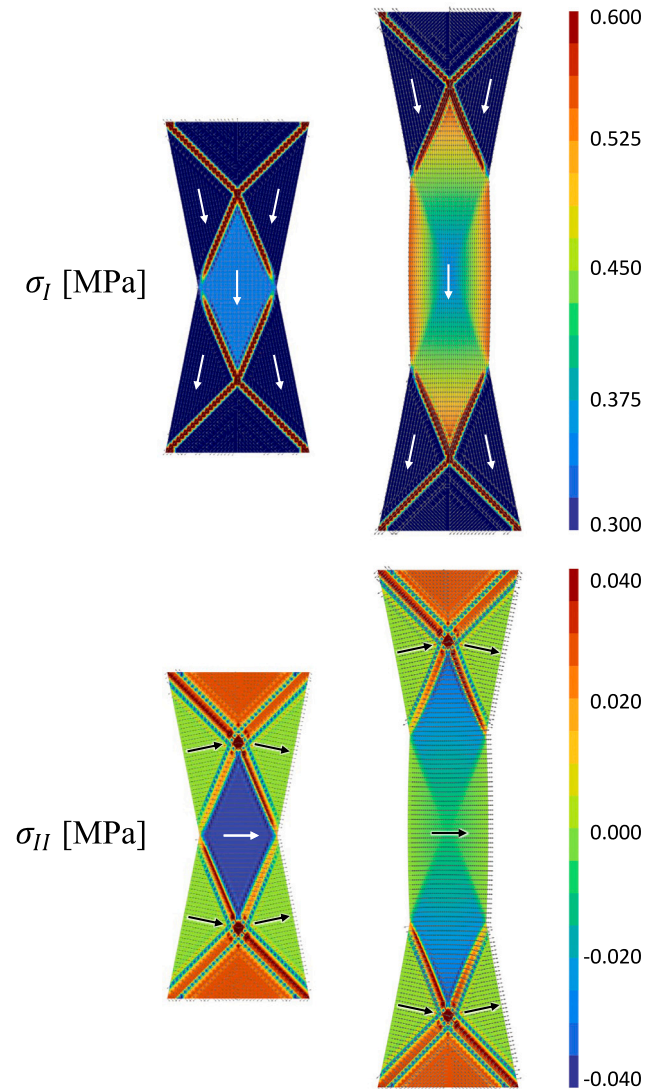| Trade name			Toray TC1225 (T300J-5HS-PAEK)
Mooney–Rivlin parameters	C_{10}	[MPa]	0
	C_{01}	[MPa]	0.0076
Viscous Cross parameters	η_0	[MPa s]	0.15
	η_∞	[MPa s]	0.05
	m	[s^{1-n}]	2.6
	n	[–]	0
Elastic fibre modulus	E_f	[GPa]	100

Fig. 8. First (top) and second (bottom) principal stress distributions resulting from the FE simulations for bias extension specimens with aspect ratios Λ of 2 and 3. The arrows indicate the corresponding orientation per region. The orientation is undefined in region C which has a hydrostatic membrane stress distribution.

3.3. Numerical validation

Numerical simulations (in which ideal trellis shear deformations can be guaranteed) were used to validate the closed form relations derived in the previous sections, thereby avoiding potential discrepancies due to slip in BE experiments. As introduced earlier, the implicit Aniform Finite Element software [28] was used to simulate BE testing of specimens with aspect ratios Λ of 2 and 3, a rate dependent material (see Table 1 for the relevant material property data) and boundary conditions such that the nominal strains and longitudinal strain rates $\dot{u}/(L_0 - W_0)$ in the central region A, with crosshead displacement rate $\dot{u}$, were synchronised and equal in both cases (see Table 2).

The area averaged shear angles were found to be equal to the values described by the kinematic relations ((1), (2)). The predicted pulling forces were slightly affected by the aspect ratio, see Fig. 7a. The principal stress resultants can be calculated from these forces according to (42), and practically coincide with the area averaged values of the FE results as shown in Fig. 7b. The underlying principal stress distributions are depicted in Fig. 8, confirming the earlier observations on non-uniformity for the larger aspect ratio. The predicted transverse stresses

are an order of magnitude smaller than the longitudinal stresses in region A, but non-zero between regions B. The simulations clearly show the effect of the boundary conditions on the transverse stresses, which are uniform for the minimum aspect ratio but zero at the free edges for larger aspect ratios. Multiplication of these membrane stresses with the local thickness leads to the principal FE stress resultants. The orientation of the principal stresses is indicated with the arrows,
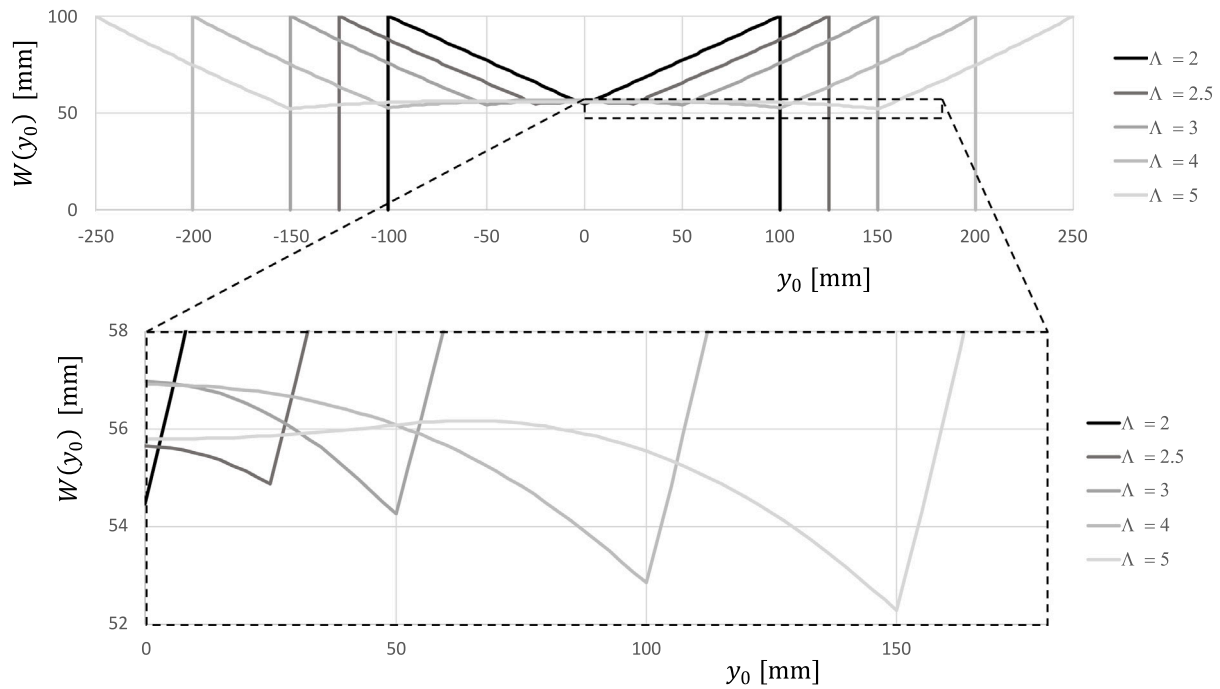
Fig. 9. Local width, plotted against the initial longitudinal coordinates y_0 (both in mm) of simulated bias extension specimens with a nominal shear angle of 45° for aspect ratios Λ from 2 to 5. Top: equidistant scaling of the full specimen lengths, bottom: scaled detail of the central regions.

Table 2

Input data for Finite Element simulations using the Aniform composites forming software. The crosshead velocities were chosen such that the nominal shear rates in the central regions A (according to the kinematic model) are equal for both cases.

Aspect ratio	2	3
length [mm]	200	300
width [mm]	100	100
number of LTR elements	6400	9600
initial fibre orientation	±45°	±45°
total displacement [mm]	30.66	61.31
crosshead velocity [mm/min]	400	800

which are seen to coincide with the bias directions as expected from theory [24]. These principal directions are undefined in region C, given the locally hydrostatic stress resultant state in this region. Also the equivalent stress resultant in (40) and its FE counterparts. calculated from the simulated principal stress resultants, are practically identical, as seen in Fig. 7c. Notably, this procedure requires no additional assumptions concerning the constitutive behaviour of the material under consideration, as long as the relevant state variables are kept equal for both aspect ratios.

The FE results also provide detailed information about the local deformations and strain field. The local width W of the simulated specimens is seen to vary along the length of region A for further variations of $\Lambda > 2$ (Fig. 9) and is logically related to the distribution of the shear angle over the width, as could be expressed by means of the linear transverse strain $\varepsilon_x = \cos \frac{1}{2}\gamma - \sin \frac{1}{2}\gamma = \sqrt{1 - \sin \gamma}$. Although the global averaged linear strain $\bar{\varepsilon}_x = W/W_0 - 1$ cannot be translated directly to the local shear angle distribution, this information may be used to validate a constitutive model.

To explore the strain field, the definition of the Green–Lagrange strain $\boldsymbol{E}^{GL} = \frac{1}{2}\left(\boldsymbol{F}^T \cdot \boldsymbol{F} - \boldsymbol{I}\right)$, with deformation gradient $\boldsymbol{F}$ and unit tensor $\boldsymbol{I}$, is generally considered to be more suitable as it cannot be corrupted by rigid body rotations. Fig. 10 shows the inplane components of $\boldsymbol{E}^{GL}$ in the global xy coordinates (coinciding with the original bias directions) on the deformed geometry of a simulated BE specimen with aspect ratio $\Lambda = 3$. The full field solution shows a distribution

directly related to the shear angles seen earlier in Fig. 2. The normal Green–Lagrange strains in x and y directions are equal but of opposite sign ($E_{xx}^{GL} = -E_{yy}^{GL} = -\sin\gamma$ for trellis shear), while the bias directions remain orthogonal such that the corresponding shear strain $E_{xy}^{GL} = 0$ throughout the domain. The predicted normal strains are maximum in absolute sense near the triple point where the regions A, B and C meet, and minimum in the centre of region A, corresponding to the shear angle distribution.

Also the predicted shear rate is non-uniform in region A, as illustrated in Fig. 11, with values close, but not identical, to the result of the kinematic model (3), $\dot{\gamma} = 0.2464\,1/s$ for the values used here (Table 2). This particular distribution is dependent on the constitutive model applied here (a nonlinearly elastic and viscous element connected in parallel [31]) and the accompanying material property data, where it should be noted that this holds for all distributions of strains and stresses in longer length specimens ($\Lambda > 2$).

Returning to the overall deformed shape of the specimen, variations in width along the length of the specimen are indisputable evidence for non-uniform shear angles. The outer contours of the specimen may also be recorded experimentally, although it will be challenging to measure such variations in specimen width with sufficient accuracy. Further, as demonstrated in [29,32,33], the effect of in-plane bending rigidity on the in-plane shear distribution in region A is opposite to the effect of compressive stresses between regions B as observed here. This implies that difficulties to show the shear gradients predicted here in an experimental setting will only increase if in-plane bending effects influence the shape of the specimen as well.

4. Discussion

The foregoing analysis confirms earlier findings that the stress states in the three regions of a uniaxial bias extension specimen of minimum length ($\Lambda = 2$) depend on two variables, although the idealised deformations can be expressed in only a single degree of freedom (e.g. clamp displacement, fibre angle or shear angle). Only measuring a single physical quantity (the externally applied pulling force) provides insufficient information to fully resolve the distribution of forces and
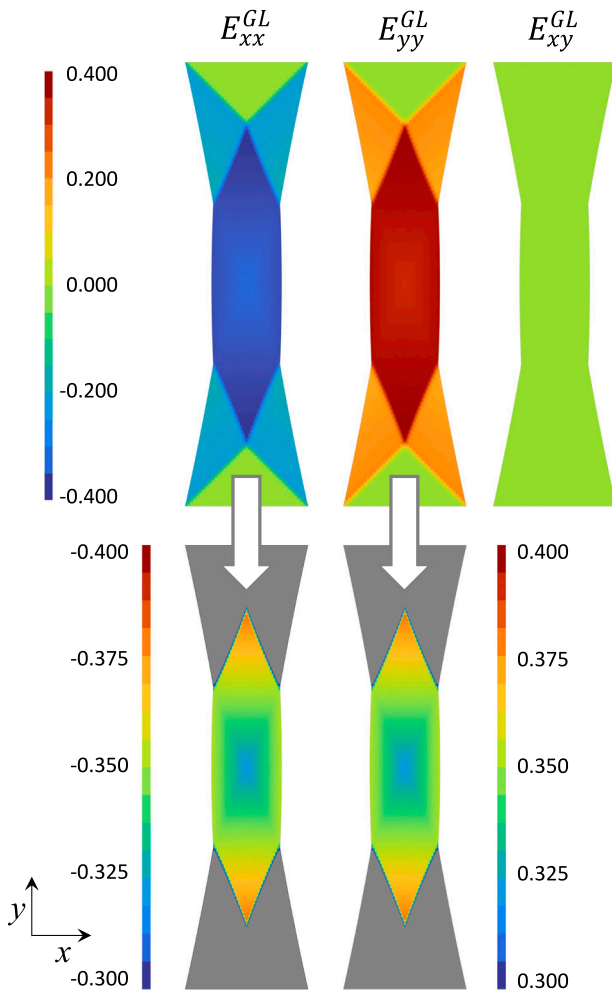
Fig. 10. Green–Lagrange strains in the original xy-coordinates and represented on the deformed geometry, from left to right: E_{xx}^{GL}, E_{yy}^{GL}, E_{xy}^{GL}, resulting from the FE simulations for a bias extension specimen with aspect ratio $\Lambda = 3$. Top row: contours over the full strain range, bottom row: contours of the normal strain components in a limited strain window (shear angles outside the range are plotted in grey).
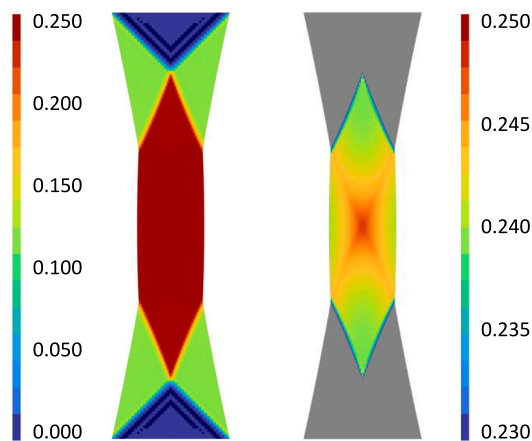

Fig. 11. Inplane shear rate $\dot{\gamma}$ [1/s], resulting from the FE simulation for a bias extension specimen with aspect ratio $\Lambda = 3$ and conditions specified in Table 2. Left: full range of shear rates, right: limited window of shear rates (shear rates outside the range are plotted in grey).

stress resultants. This requires additional information or assumptions, e.g. by measuring specimens of different lengths or any of the other

forces (complicating the experiment) or by assuming the functional relation between the equivalent stress resultant and selected state variables (such as assuming independency of rate and fibre tension, thereby limiting the applicability of the result).

In general, the minimum length solution (i.e. $\Lambda = 2$) of the equivalent stress resultant $\tilde{\tau}^A$ involves non-zero transverse stresses in the central region A (in our experience generally compressive) such that the equivalent stress resultant cannot be determined directly from the pulling force data and differs from the long length solution ($\Lambda \to \infty$) of purely uniaxial tension. The exception to the rule is the artificial constitutive equation $\tilde{\tau} = \frac{c}{\cos \gamma}$ with c as an arbitrary constant which may be interpreted as the yield parameter in a rigid plastic model with strain hardening, for which the transverse force $N_A = 0$ throughout the test, as can be found from (30). For specimens of intermediate length, these different boundary conditions must lead to non-uniform stresses and strains in region A, which disqualifies List 4 and makes such sizes less attractive for material characterisation purposes. However, when the long length solution applies and the central zone deforms uniformly (e.g. without wrinkling and gravitational effects), then $\tilde{\tau}^A$ follows directly from the pulling force, leading to an unambiguous relation with the strain and strain rate, without the need for further measurements or assumptions. Slip boundary conditions [34], alternative clamping [9] and wrinkle mitigation [35] may be instrumental to achieve a workable solution.

The discrete step in shear stresses between the regions, following from the ideal kinematics, leads to localised high fibre tension, being maximum at the clamped edge (T_4). In practice, small but finite in-plane bending rigidity of the reinforcement will distribute the shear difference and this tension over a larger area than one infinitely thin fibre. Nonetheless, this is an obvious cause for the experimental problems with specimen clamping as reported by different authors. Numerical simulations employing continuum models without discrete fibres (e.g. truss elements) will show concentrated stresses on these boundaries, not converging with mesh refinement unless in-plane bending rigidity (or another mechanism causing smoothening) is included in these models, smearing out the discrete step in shear stress over these boundaries.

Reviewing the analysis presented here, it appears that one single assumption, which was usually taken implicitly, has led to confusion as its consequence was usually overlooked. The deformations of the central region A cannot be assumed to be homogeneous for arbitrary length-to-width ratios, which needs to be taken into account for accurate material characterisation experiments.

As a final remark, also the term "uniaxial bias extension" can easily lead to confusion and should be used with care. Although the external loading is indeed uniaxial for this test, the stress state in the central region is mostly biaxial instead, starting at $\tau_x^A = -\frac{1}{3}\tau_y^A$ in the limit of linear material behaviour for small deformations.

5. Conclusion

A static equilibrium analysis was presented to clarify the effect of specimen length on the results of the bias extension test. It was demonstrated that uniform deformations are to be expected in each region for minimum length specimens ($\Lambda = 2$), but also that nonhomogeneous boundary conditions are imposed on the central region in specimens of a longer length, due to which the deformations in this central region should not be assumed to be uniform. The minimum length solution of the forces and stress resultants depends on two variables of which usually only one is measured (the pulling force) while e.g. the transverse force is unknown. Additional information is required to fully resolve the stress state for this case, e.g. by assuming pre-selected constitutive behaviour, or with further experimental data: for other aspect ratios, with extra instrumentation or other boundary conditions. The problem of unknown transverse stresses is avoided by using very long specimens ($\Lambda \to \infty$), but these are subject to wrinkling and

possibly slumping of the specimen under its own gravitational loading. Specimens of intermediate length exhibit strain gradients in the central region, inherently hampering high precision material characterisation.

Finally, the analysis results show that the major part of the pulling load is carried by the outer fibres, explaining the clamping issues experienced during testing. These conclusions emphasise the need for critical preparation, execution and interpretation of bias extension experiments if highly accurate material property data are to be extracted from the measurement results.

CRediT authorship contribution statement

Remko Akkerman: Conceptualization, Methodology, Validation, Formal analysis, Writing – original draft, Writing – review & editing, Visualization. **Dennis Brands:** Validation, Writing – review & editing, Visualization. **Wouter J.B. Grouve:** Conceptualization, Writing – review & editing.

Declaration of competing interest

The authors declare that they have no known competing financial interests or personal relationships that could have appeared to influence the work reported in this paper.

Data availability

Data will be made available on request.

Acknowledgements

Appendix

Explicit relations for the full field stress resultants are useful for validation of numerical simulations of the BE test. As shown earlier [24], the stress resultant tensor $\boldsymbol{\tau}$ at any point in a thin fabric material can be decomposed into three physically relevant components: the constitutively determined equivalent stress resultant $\tilde{\tau}$ and two stress resultants in the fibre directions $\mathcal{T}_i = \boldsymbol{\tau} : \boldsymbol{A}_i$ $(i = 1, 2)$ which do not depend on elongation as the fibres are considered inextensible, and hence can only be determined based on equilibrium considerations. In each of the regions of the BE specimen the fibres tensions are equal in both directions so $\mathcal{T}_1 = \mathcal{T}_2 \equiv \mathcal{T}$, with which the stress resultant tensor can be decomposed (using the bias directions as the coordinate axes) into

$$
[\boldsymbol{\tau}] = \frac{\mathcal{T}}{1 + \sin^2 \theta} \begin{bmatrix} 1 + \sin \theta & 0 \\ 0 & 1 - \sin \theta \end{bmatrix} + \\
+ \frac{\tilde{\tau} \cos \theta}{1 + \sin^2 \theta} \begin{bmatrix} 1 - \sin \theta & 0 \\ 0 & -1 - \sin \theta \end{bmatrix},
\tag{43}
$$

with θ as the local shear angle (different for the three regions in this particular case).

The equivalent stress resultant in region C is zero. The remaining relevant stress resultant terms can be expressed as a linear combination of the equivalent stress resultants in regions A and B,

$$
\mathcal{T}^{\mathsf{A}} = 2 \tan \gamma \cdot \tilde{\tau}^{\mathsf{A}} + \cos \tfrac{1}{2}\gamma \cdot \frac{1 + \sin^2 \gamma}{\cos^2 \gamma} \cdot \tilde{\tau}^{\mathsf{B}},
$$

$$
\mathcal{T}^{\mathsf{B}} = \frac{(1 + \sin \tfrac{1}{2}\gamma)\left((\sqrt{2} - 1)\cos \tfrac{1}{2}\gamma - \sin \tfrac{1}{2}\gamma\right)}{1 - (\sqrt{2} - 1)\cos \tfrac{1}{2}\gamma - \sin \tfrac{1}{2}\gamma} \cdot \tilde{\tau}^{\mathsf{B}},
\tag{44}
$$

$$
\mathcal{T}^{\mathsf{C}} = \cos \tfrac{1}{2}\gamma \cdot \tilde{\tau}^{\mathsf{B}},
$$

indicating proportionality between $\mathcal{T}^{\mathsf{B}}$, $\mathcal{T}^{\mathsf{C}}$ and $\tilde{\tau}^{\mathsf{B}}$ at a given shear angle.

References

[1] Cao J, Akkerman R, Boisse P, Chen J, Cheng HS, de Graaf EF, et al. Characterization of mechanical behavior of woven fabrics: Experimental methods and benchmark results. Composites A 2008;39(6). http://dx.doi.org/10.1016/j.compositesa.2008.02.016.

[2] Wang J, Page JR, Paton R. Experimental investigation of the draping properties of reinforcement fabrics. Compos Sci Technol 1998;58(2):229–37. http://dx.doi.org/10.1016/S0266-3538(97)00115-2.

[3] Potter K. Bias extension measurements on cross-plied unidirectional prepreg. Composites A 2002;33(1):63–73. http://dx.doi.org/10.1016/S1359-835X(01)00057-4.

[4] Larberg Y, Åkermo M. In-plane deformation of multi-layered unidirectional thermoset prepreg - Modelling and experimental verification. Composites A 2014;56:203–12. http://dx.doi.org/10.1016/j.compositesa.2013.10.005.

[5] Brands D, Wijskamp S, Grouve WJB, Akkerman R. In-plane shear characterization of unidirectional fiber reinforced thermoplastic tape using the bias extension method. Front Mater 2022;9(June):1–13. http://dx.doi.org/10.3389/fmats.2022.863952.

[6] Bel S, Boisse P, Dumont F. Analyses of the deformation mechanisms of non-crimp fabric composite reinforcements during preforming. Appl Compos Mater 2012;19(3–4):513–28. http://dx.doi.org/10.1007/s10443-011-9207-x.

[7] Barbagallo G, Madeo A, Azehaf I, Giorgio I, Morestin F, Boisse P. Bias extension test on an unbalanced woven composite reinforcement: Experiments and modeling via a second-gradient continuum approach. J Compos Mater 2017;51(2):153–70. http://dx.doi.org/10.1177/0021998316643577.

[8] Weissenberg K. 5-The use of a trellis model in the mechanics of homogeneous materials. J Text Inst Trans 1949;40(2):T89–110. http://dx.doi.org/10.1080/19447024908659443.

[9] Chadwick GE, Shorter SA, Weissenberg K. 6-A trellis model for the application and study of simple pulls in textile materials. J Text Inst Trans 1949;40(2):T111–60. http://dx.doi.org/10.1080/19447024908659444.

[10] Cooper DNE. A bias extension test. Text Res J 1963;33(4):315–7. http://dx.doi.org/10.1177/004051756303300408.

[11] Kilby WF. 2-Planar stress-strain relationships in woven fabrics. J Text Inst Trans 1963;54(1):T9–27. http://dx.doi.org/10.1080/19447026308659910.

[12] Skelton J. Fundamentals of fabric shear. Text Res J 1976;46(12):862–9. http://dx.doi.org/10.1177/004051757604601202.

[13] Bassett RJ, Postle R, Pan N. Experimental methods for measuring fabric mechanical properties: A review and analysis. Text Res J 1999;69(11):866–75. http://dx.doi.org/10.1177/004051759906901111.

[14] Boisse P, Hamila N, Guzman-Maldonado E, Madeo A, Hivet G, Dell'Isola F. The bias-extension test for the analysis of in-plane shear properties of textile composite reinforcements and prepregs: A review. Int J Mater Form 2017;10(4):473–92. http://dx.doi.org/10.1007/s12289-016-1294-7.

[15] Spivak SM, Treloar LRG. The behavior of fabrics in shear: Part III: The relation between bias extension and simple shear. Text Res J 1968;38(9):963–71. http://dx.doi.org/10.1177/004051756803800911.

[16] Lebrun G, Bureau MN, Denault J. Evaluation of bias-extension and picture-frame test methods for the measurement of intraply shear properties of PP/glass commingled fabrics. Compos Struct 2003;61(4):341–52. http://dx.doi.org/10.1016/S0263-8223(03)00057-6.

[17] Harrison P, Clifford MJ, Long AC. Shear characterisation of viscous woven textile composites: A comparison between picture frame and bias extension experiments. Compos Sci Technol 2004;64(10–11):1453–65. http://dx.doi.org/10.1016/j.compscitech.2003.10.015.

[18] Harrison P, Wiggers J, Long AC. Normalization of shear test data for rate-independent compressible fabrics. J Compos Mater 2008;42(22):2315–44. http://dx.doi.org/10.1177/0021998308095367.

[19] Launay J, Hivet G, Duong AV, Boisse P. Experimental analysis of the influence of tensions on in plane shear behaviour of woven composite reinforcements. Compos Sci Technol 2008;68(2):506–15. http://dx.doi.org/10.1016/j.compscitech.2007.06.021.

[20] Komeili M, Milani AS. An elaboration on the shear characterization of dry woven fabrics using trellising tests. Polym Compos 2013;34(3):359–67. http://dx.doi.org/10.1002/pc.22347.

[21] Haghi Kashani M, Hosseini A, Sassani F, Ko FK, Milani AS. The role of intra-yarn shear in integrated multi-scale deformation analyses of woven fabrics: A critical review. Crit Rev Solid State Mater Sci 2018;43(3):213–32. http://dx.doi.org/10.1080/10408436.2017.1342597.

[22] Xiao S, Gao H, Soulat D, Wang P. A revised model of kinematic analysis on in-plane shearing behaviour of biaxial fabrics in bias extension test. Composites A 2022;163(August):107251. http://dx.doi.org/10.1016/j.compositesa.2022.107251.

[23] Prodromou AG, Chen J. On the relationship between shear angle and wrinkling of textile composite preforms. Composites A 1997;28(5):491–503. http://dx.doi.org/10.1016/S1359-835X(96)00150-9.

[24] Akkerman R. A continuum mechanics analysis of shear characterisation methods. Composites A 2018;109:131–40. http://dx.doi.org/10.1016/j.compositesa.2018.02.036.

[25] Härtel F, Harrison P. Evaluation of normalisation methods for uniaxial bias extension tests on engineering fabrics. Composites A 2014;67:61–9. http://dx.doi.org/10.1016/j.compositesa.2014.08.011.

[26] Hivet G, Duong AV. A contribution to the analysis of the intrinsic shear behavior of fabrics. J Compos Mater 2011;45(6):695–716. http://dx.doi.org/10.1177/0021998310382315.

[27] Harrison P, Härtel F. Erratum: 'Evaluation of normalisation methods for uniaxial bias extension tests on engineering fabrics' (Composites: Part A (2016) 80 (104-106)). Composites A 2016;80:104–6. http://dx.doi.org/10.1016/j.compositesa.2015.10.013.

[28] AniForm Engineering BV. AniForm. 2022-09-16, version 4.2.0, https://www.aniform.com.

[29] Harrison P, Alvarez MF, Anderson D. Towards comprehensive characterisation and modelling of the forming and wrinkling mechanics of engineering fabrics. Int J Solids Struct 2018;154:2–18. http://dx.doi.org/10.1016/j.ijsolstr.2016.11.008.

[30] Harrison P, Yu WR, Long AC. Rate dependent modelling of the forming behaviour of viscous textile composites. Composites A 2011;42(11):1719–26. http://dx.doi.org/10.1016/j.compositesa.2011.07.026.

[31] Haanappel SP, Ten Thije RHW, Sachs U, Rietman B, Akkerman R. Formability analyses of uni-directional and textile reinforced thermoplastics. Composites A 2014;56:80–92. http://dx.doi.org/10.1016/j.compositesa.2013.09.009.

[32] Harrison P. Modelling the forming mechanics of engineering fabrics using a mutually constrained pantographic beam and membrane mesh. Composites A 2016;81:145–57. http://dx.doi.org/10.1016/j.compositesa.2015.11.005.

[33] Giorgio I, Harrison P, Dell'Isola F, Alsayednoor J, Turco E. Wrinkling in engineering fabrics: A comparison between two different comprehensive modelling approaches. Proc R Soc 2018;474(2216):20180063. http://dx.doi.org/10.1098/rspa.2018.0063.

[34] Rashidi A, Montazerian H, Milani AS. Slip-bias extension test: A characterization tool for understanding and modeling the effect of clamping conditions in forming of woven fabrics. Compos Struct 2021;260(January):113529. http://dx.doi.org/10.1016/j.compstruct.2020.113529.

[35] Harrison P, Taylor E, Alsayednoor J. Improving the accuracy of the uniaxial bias extension test on engineering fabrics using a simple wrinkle mitigation technique. Composites A 2018;108(January):53–61. http://dx.doi.org/10.1016/j.compositesa.2018.02.025.